

# MIGHTY: Hermite Spline-based Efficient Trajectory Planning

Kota Kondo<sup>1</sup>, Yuwei Wu<sup>2</sup>, Vijay Kumar<sup>2</sup>, Jonathan P. How<sup>1</sup>

**Abstract**—Hard-constraint trajectory planners often rely on commercial solvers and demand substantial computational resources. Existing soft-constraint methods achieve faster computation, but either (1) decouple spatial and temporal optimization or (2) restrict the search space. To overcome these limitations, we introduce **MIGHTY**, a Hermite spline-based planner that performs spatiotemporal optimization while fully leveraging the continuous search space of a spline. In simulation, **MIGHTY** achieves a 9.3% reduction in computation time and a 13.1% reduction in travel time over state-of-the-art baselines, with a 100% success rate. In hardware, **MIGHTY** completes multiple high-speed flights up to 6.7 m/s in a cluttered static environment and long-duration flights with dynamically added obstacles.

## SUPPLEMENTARY MATERIAL

**Video:** <https://youtu.be/Pvb-VPUDLvg>

**Code:** <https://github.com/mit-acl/mighty.git>

## I. INTRODUCTION

Trajectory planning for autonomous navigation has been extensively studied, with a wide variety of parameterizations and formulations [3], [6], [7], [9], [12], [14]–[17], [19]–[23]. For real-world deployment, fast trajectory generation is critical to ensure agile and safe flight in cluttered and dynamic environments. Approaches that use hard constraints [3], [6], [9], [12], [16] explicitly enforce safety and physical feasibility but often rely on computationally intensive solvers, making them difficult to deploy for high-frequency replanning on onboard processors. Soft-constraint planners such as EGO-Planner [22], RAPTOR [21], and SUPER [14] achieve faster convergence and lower computational cost. Some jointly optimize path geometry and timing within a single nonlinear formulation [14], [19], while others separate path generation and time allocation into two stages [15], [21]. In general, increasing the number of decision variables, such as control points, segment durations, or derivative values, can improve performance but also enlarges the optimization problem and increases computation time. To balance efficiency and performance, recent work has explored alternative trajectory representations and optimization strategies, and building on these ideas, the following introduces our Hermite spline-based planner, **MIGHTY**.

### A. Review of Unconstrained Frameworks

Differential flatness [4] enables efficient optimization of quadrotor trajectories by parameterizing the flat output ( $x$ ,  $y$ ,  $z$ , yaw) and their derivatives. Given fixed timestamps at trajectory waypoints, minimum control effort (e.g., jerk/snap) problems using piecewise polynomial representation can be formulated as quadratic programs (QPs), which are convex

and can be solved efficiently [12]. However, when segment durations are included as optimization variables (time allocation), the resulting joint problem becomes substantially more complex, yielding a nonlinear program (NLP) that is often ill-conditioned because of the coupling between spatial and temporal variables.

One common strategy is to decouple the problem into two stages and relax hard constraints to adopt unconstrained formulations. For example, Richter et al. [15] apply piecewise 9<sup>th</sup>-order polynomials on the flat outputs with endpoint derivatives as decision variables. The trajectory optimization follows a two-stage process: an unconstrained QP minimizes snap to ensure smoothness, followed by a gradient-based time allocation step that adjusts the total trajectory duration. Collision avoidance is addressed heuristically by inserting mid-segment waypoints whenever a segment intersects obstacles, which triggers repeated QP solves until a collision-free solution is found. This approach is extended in [1] by improving numerical stability and incorporating additional soft state constraint costs to further ensure trajectory feasibility. Similarly, the work in [13] adapts this framework to achieve local real-time replanning, using endpoint derivatives as optimization variables, which minimizes snap and collisions using a potential cost function based on Euclidean signed distance field (ESDF).

Another standard unconstrained framework uses B-splines for trajectory representation, with time-related variables encoded in a knot vector. B-splines offer inherent smoothness, local control, and the convex hull property, which enables efficient collision checking and enforces dynamic feasibility [16], [20]–[22]. Zhou et al. [20] parameterize trajectories as non-uniform cubic B-splines initialized from kinodynamic A\* paths. The nonlinear optimization minimizes the cost considering smoothness, a repulsive collision potential from an Euclidean distance field (EDF), and soft penalties on derivative control points exceeding maximum velocity and acceleration. Finally, an iterative time-adjustment method rescales knot spans of the non-uniform spline to guarantee dynamic feasibility. EGO-Planner [22] and RAPTOR [21] simplify the representation by using uniform B-splines with fixed knot spans, leveraging convex hull properties to enforce velocity, acceleration, and jerk constraints directly on control points. EGO-Planner optimizes trajectories via a quasi-Newton solver (L-BFGS) [8] for fast gradient-based convergence, with an additional time-reallocation and anisotropic curve-fitting refinement stage that resizes knot spans and fits a new spline to ensure feasibility and smoothness. RAPTOR also employs a two-stage process: a closed-form QP warm-start for initial smoothness, followed by a nonlinear refinement phase that penalizes collision via an ESDF and ensures dynamic limits via control point constraints.

To further improve efficiency, alternative representations

<sup>1</sup>Department of Aeronautics and Astronautics, Massachusetts Institute of Technology ({kkondo, jhow}@mit.edu). <sup>2</sup>Department of Electrical and Systems Engineering, University of Pennsylvania ({yuweiwu, kumar}@seas.upenn.edu).

TABLE I. State-of-the-art Unconstrained UAV Trajectory Planners

Method	Representation	Variables	Time Opt.	Search Space	Local Control
<b>Polynomial</b> [15] (2016)	9th-order polynomial	endpoint derivs, time	decoupled	limited polynomial+time space	yes
<b>Robust</b> [20] (2019)	non-uniform cubic B-spline	B-spline cntrl pts, time	decoupled	limited polynomial+time space	yes
<b>EGO-Planner</b> [22] (2021)	uniform cubic B-spline	B-spline cntrl pts	fixed	limited polynomial+time space	yes
<b>RAPTOR</b> [21] (2021)	uniform cubic B-spline	B-spline cntrl pts	fixed	limited polynomial+time space	yes
<b>MINCO class</b> [14], [19], [23] (2022, 2022, 2025)	MINCO	pos., time	joint	limited polynomial+time space (MINCO manifold)	no
<b>MIGHTY (proposed)</b>	Hermite	Hermite cntrl pts, time.	joint	full polynomial+time space	yes

of polynomial variables have been explored. Wang et al. [18] employ an explicit diffeomorphism between coefficients and boundary derivatives, with a linear-complexity scheme for gradient evaluation towards coefficients. Built on this, MINCO [19] parametrizes a segmented trajectory as piecewise polynomials, where coefficients are analytically determined by intermediate waypoints and segment durations, which are jointly optimized. A linear-complexity solver then constructs the minimum-control trajectory that minimizes the integrated control effort (e.g., jerk/snap) subject to flatness boundary conditions. Spatiotemporal deformation leverages smooth diffeomorphisms and convex constraint-elimination maps to enforce arbitrary collision and state-input constraints. However, although MINCO provides an elegant and computationally efficient formulation, since it directly maps intermediate waypoints and segment durations to polynomial coefficients using the optimality conditions of the optimal control-effort problem [19], the search is, by construction, restricted to a low-dimensional manifold, potentially limiting flexibility when additional constraints or objectives are introduced. Additionally, because MINCO determines all polynomial coefficients by solving a single banded linear system subject to high-order continuity and optimality conditions, any change to one intermediate waypoint or segment duration generally changes the entire solution. In other words, MINCO does not have strict local control, meaning a small change to one waypoint or duration can propagate to many segments, complicating per-segment constraint handling for local changes. EGO-Swarm2 [23] and SUPER [14] both adopt MINCO to compactly parameterize trajectories, with SUPER further optimizing exploratory and backup trajectories in each replanning cycle to balance aggressiveness and guaranteed safety. However, the intrinsic coupling within the MINCO formulation remains a limitation. MIGHTY aims to address this by optimizing over a higher-dimensional representation that preserves local control and improves flexibility for handling complex constraints.

### B. MIGHTY Contributions

Summarizing the discussion above, direct unconstrained higher-order polynomial representations [15] are typically too slow for real-time planning. Uniform or Non-uniform splines [20]–[22] can generate trajectories faster compared to spatiotemporal joint optimization; however, they can generate sub-optimal trajectories due to decoupled time adjustment. Waypoint-and-duration-based parameterizations [14], [19], [23] are restricted to a low-dimensional manifold, and a

small change in one waypoint propagates globally through all polynomial coefficients. This is undesirable for real-time planning because it potentially complicates constraint/cost handling and slows down convergence.

To address the limitations of existing soft-constraint planners, MIGHTY uses a Hermite-spline representation and an unconstrained nonlinear optimizer that searches directly over spatial waypoints, endpoint derivatives, and segment durations. A Hermite spline representation also guarantees continuity without global coefficient coupling. As such, the key contributions of the paper are:

- 1) **Hermite Spline Planner:** Joint spatiotemporal optimization in a single solve, fully leveraging the continuous search space of Hermite splines and supporting local control of trajectory shape. The approach, MIGHTY, achieves fast solve times and superior performance.
- 2) **Comprehensive Simulation Study:** We benchmark in both simple and complex scenes, comparing against state-of-the-art methods in static environments and validating safe behavior in dynamic environments. MIGHTY achieves **9.3 %** reduction in computation time and **13.1 %** reduction in travel time in trajectory representation benchmarking, and it achieves the shortest travel time and path length while maintaining the **100 %** success rate.
- 3) **Extensive Hardware Experiments:** Long-duration flights, high-speed flights, and dynamic obstacle avoidance scenarios using a LiDAR-based perception and localization system. MIGHTY achieves collision-free long-duration flights and a top speed of **6.7 m/s** in high-speed flight experiments.

## II. HERMITE SPLINE

This section introduces the Hermite-spline notation used in MIGHTY’s formulation. MIGHTY uses a degree- $d$  Hermite spline with  $M$  segments. For odd degree  $d = 2k + 1$ , each segment is parameterized by the knot values of the position and its derivatives up to order  $k$ . For example, a quintic Hermite spline ( $d = 5$ ,  $k = 2$ ) specifies position, velocity, and acceleration. Across knots, a Hermite spline automatically guarantees  $C^k$  continuity by sharing the knot values. Although Hermite splines apply in any dimension, we work in  $\mathbb{R}^3$  for quadrotor planning and use  $d = 5$  in this paper. For each segment  $s = 0, \dots, M - 1$ , we define a normalized time variable  $\tau_s \in [0, 1]$  on segment  $s$  as  $\tau_s = (t - t_s)/T_s \in [0, 1]$ . Then each segment can be denoted as:  $\mathbf{x}(t) = \mathbf{x}_s(\tau_s)$ ,  $t \in [t_s, t_{s+1}]$ , where  $t_s := \sum_{r=0}^{s-1} T_r$ ,

and  $T_s$  is the duration of segment  $s$ . Then we write

$$\mathbf{x}_s(\tau_s) = \sum_{k=0}^5 h_k(\tau_s) \mathbf{H}_{s,k}, \quad (1)$$

where  $\mathbf{H}_{s,0} = \mathbf{p}_s$ ,  $\mathbf{H}_{s,1} = T_s \mathbf{v}_s$ ,  $\mathbf{H}_{s,2} = \frac{1}{2} T_s^2 \mathbf{a}_s$ ,  $\mathbf{H}_{s,3} = \mathbf{p}_{s+1}$ ,  $\mathbf{H}_{s,4} = T_s \mathbf{v}_{s+1}$ ,  $\mathbf{H}_{s,5} = \frac{1}{2} T_s^2 \mathbf{a}_{s+1}$ . where  $h_k(\tau_s)$  are the standard quintic Hermite basis functions. The  $\mathbf{p}_i, \mathbf{v}_i, \mathbf{a}_i \in \mathbb{R}^3$  ( $i = 0, \dots, M$ ) and  $T_s > 0$  ( $s = 0, \dots, M-1$ ) are the interior knot positions, velocities, accelerations, and segment durations, respectively.

### III. MIGHTY

#### A. Decision Variables

As shown in Section II, the knot states  $\mathbf{p}_i, \mathbf{v}_i, \mathbf{a}_i$  ( $i = 0, \dots, M$ ) and segment durations  $T_s$  ( $s = 0, \dots, M-1$ ) fully determine the trajectory. Thus we optimize the interior positions, velocities, accelerations, and per-segment durations:

$$\mathbf{z} = [\mathbf{p}_1^\top, \mathbf{v}_1^\top, \mathbf{a}_1^\top, \dots, \mathbf{p}_{M-1}^\top, \mathbf{v}_{M-1}^\top, \mathbf{a}_{M-1}^\top, T_0, \dots, T_{M-1}]^\top$$

with fixed boundary states  $(\mathbf{p}_0, \mathbf{v}_0, \mathbf{a}_0)$  and  $(\mathbf{p}_M, \mathbf{v}_M, \mathbf{a}_M)$ .

To keep the optimization unconstrained while enforcing certain requirements (e.g.,  $T_s > 0$ ), we apply diffeomorphism, such as  $T_s = \phi(\sigma_s)$  with  $\phi(\sigma) = e^\sigma$ ,  $\sigma_s \in \mathbb{R}$ . We also find that optimizing raw derivative knots  $(\mathbf{v}_i, \mathbf{a}_i)$  can be numerically unstable. Section III-D introduces scalings that improve stability without changing the optimum. For clarity, the formulas below are written in terms of the original variables  $(\mathbf{p}_s, \mathbf{v}_s, \mathbf{a}_s, T_s)$ ; applying a diffeomorphism only inserts chain-rule factors in the gradients.

#### B. Representations

Given the quintic Hermite segment in Eq. (1), a smooth cost can be expressed in terms of the raw Hermite variables  $(\mathbf{p}_s, \mathbf{v}_s, \mathbf{a}_s, \mathbf{p}_{s+1}, \mathbf{v}_{s+1}, \mathbf{a}_{s+1}, T_s)$ . However, evaluating costs and gradients directly in Hermite form can be computationally expensive, and other representations, such as Bézier curve, can be more efficient.

For instance, a Bézier curve allows efficient evaluation of the trajectory and its derivatives at arbitrary sample points. A degree- $n$  Bézier segment is written as  $\mathbf{x}(u) = \sum_{i=0}^n B_i^n(u) \mathbf{c}_i$ ,  $u \in [0, 1]$ , where the vectors  $\mathbf{c}_i$  are the Bézier control points, and the Bernstein basis polynomials are  $B_i^n(u) = \binom{n}{i} u^i (1-u)^{n-i}$ ,  $i = 0, \dots, n$ . Because evaluation is just a weighted sum of control points with weights  $B_i^n(u)$ , sampling reduces to a few dot products with small, reusable tables. Then each sample is a small dot product: positions use the  $B_i^5$  table, and derivatives use the degree-reduced Bernstein weights. Since these tables are tiny and shared across iterations, and each dot product has only 6, 5, 4, 3 terms (for degree 5 down to 2), this is faster and numerically steadier than recomputing higher-order Hermite polynomials and their derivatives at every sample.

Although Bézier representation has these computational advantages, note that Bézier control points do not enforce cross-segment continuity by themselves. On the other hand, Hermite variables guarantee  $C^k$  continuity across segments by construction. Therefore, it is often advantageous to optimize in the Hermite parameterization while evaluating cost terms in the Bézier basis to exploit its computational benefits.

In our simulations and hardware experiments, we optimize over Hermite and evaluate costs in Bézier; however, in general, MIGHTY does not require Bézier for cost evaluation.

#### C. Objective and Closed-Form Gradient

To make the formulation basis-independent, we express the objective and its gradients with respect to a generic control-point (or coefficient) vector  $\mathbf{c}$ , independent of the chosen parameterization (Hermite end states, Bézier control points, etc.). As a concrete example, the affine map between Hermite and Bézier on segment  $s$  is

$$\begin{aligned} \mathbf{c}_{s,0} &= \mathbf{p}_s, \quad \mathbf{c}_{s,1} = \mathbf{p}_s + \frac{T_s}{5} \mathbf{v}_s, \quad \mathbf{c}_{s,2} = \mathbf{p}_s + \frac{2T_s}{5} \mathbf{v}_s + \frac{T_s^2}{20} \mathbf{a}_s, \\ \mathbf{c}_{s,3} &= \mathbf{p}_{s+1} - \frac{2T_s}{5} \mathbf{v}_{s+1} + \frac{T_s^2}{20} \mathbf{a}_{s+1}, \quad \mathbf{c}_{s,4} = \mathbf{p}_{s+1} - \frac{T_s}{5} \mathbf{v}_{s+1}, \\ \mathbf{c}_{s,5} &= \mathbf{p}_{s+1}. \end{aligned} \quad (2)$$

Let  $\mathbf{c}_s = [\mathbf{c}_{s,0}^\top \dots \mathbf{c}_{s,5}^\top]^\top$  and  $\mathbf{y}_s = [\mathbf{p}_s^\top, \mathbf{v}_s^\top, \mathbf{a}_s^\top, \mathbf{p}_{s+1}^\top, \mathbf{v}_{s+1}^\top, \mathbf{a}_{s+1}^\top]^\top$ , so  $\mathbf{c}_s = C(T_s) \mathbf{y}_s$ . Let the total objective be  $J(\mathbf{z}) = \sum_{s=0}^{M-1} J_s(\mathbf{c}_s)$ . To obtain  $\partial J / \partial \mathbf{z}$ , we first compute the derivatives w.r.t  $\mathbf{y}_s$  and  $T_s$ , then apply the chain rule back to  $\mathbf{z}$ . Denote  $\mathbf{g}_{\mathbf{c}_s} \equiv \partial J_s / \partial \mathbf{c}_s$  and the explicit time derivative  $\partial J_s / \partial T_s|_{\text{explicit}}$ . Since  $\partial \mathbf{c}_s / \partial \mathbf{y}_s = C(T_s)$ , the chain rule yields

$$\frac{\partial J_s}{\partial \mathbf{y}_s} = C(T_s)^\top \mathbf{g}_{\mathbf{c}_s}, \quad (3)$$

$$\frac{\partial J_s}{\partial T_s} = \frac{\partial J_s}{\partial T_s}|_{\text{explicit}} + \mathbf{g}_{\mathbf{c}_s}^\top \frac{\partial \mathbf{c}_s}{\partial T_s}. \quad (4)$$

Note that the explicit time derivative  $\partial J_s / \partial T_s|_{\text{explicit}}$  comes from factors like  $T_s^5$  in smoothness integrals. Using Eq. (2), the entries of  $C(T_s)$  are simple constants, so Eq. (3) expands to the following closed-form expressions:

$$\begin{aligned} \nabla_{\mathbf{p}_s} J_s &= \mathbf{g}_{\mathbf{c}_{s,0}} + \mathbf{g}_{\mathbf{c}_{s,1}} + \mathbf{g}_{\mathbf{c}_{s,2}}, \quad \nabla_{\mathbf{v}_s} J_s = \frac{T_s}{5} \mathbf{g}_{\mathbf{c}_{s,1}} + \frac{2T_s}{5} \mathbf{g}_{\mathbf{c}_{s,2}}, \\ \nabla_{\mathbf{a}_s} J_s &= \frac{T_s^2}{20} \mathbf{g}_{\mathbf{c}_{s,2}}, \quad \nabla_{\mathbf{p}_{s+1}} J_s = \mathbf{g}_{\mathbf{c}_{s,3}} + \mathbf{g}_{\mathbf{c}_{s,4}} + \mathbf{g}_{\mathbf{c}_{s,5}}, \\ \nabla_{\mathbf{v}_{s+1}} J_s &= -\frac{2T_s}{5} \mathbf{g}_{\mathbf{c}_{s,3}} - \frac{T_s}{5} \mathbf{g}_{\mathbf{c}_{s,4}}, \quad \nabla_{\mathbf{a}_{s+1}} J_s = \frac{T_s^2}{20} \mathbf{g}_{\mathbf{c}_{s,3}}. \end{aligned}$$

And  $\partial \mathbf{c}_s / \partial T_s$  used in the coefficient path in Eq. (4) can be computed in closed form as

$$\begin{aligned} \frac{\mathbf{c}_{s,0}}{T_s} &= 0, \quad \frac{\mathbf{c}_{s,1}}{T_s} = \frac{1}{5} \mathbf{v}_s, \quad \frac{\mathbf{c}_{s,2}}{T_s} = \frac{2}{5} \mathbf{v}_s + \frac{T_s}{10} \mathbf{a}_s, \\ \frac{\mathbf{c}_{s,3}}{T_s} &= -\frac{2}{5} \mathbf{v}_{s+1} + \frac{T_s}{10} \mathbf{a}_{s+1}, \quad \frac{\mathbf{c}_{s,4}}{T_s} = -\frac{1}{5} \mathbf{v}_{s+1}, \quad \frac{\mathbf{c}_{s,5}}{T_s} = 0. \end{aligned} \quad (5)$$

Therefore, to obtain the gradient, we need to compute  $\mathbf{g}_{\mathbf{c}_s}$  and  $\partial J_s / \partial T_s|_{\text{explicit}}$ . Here we present two types of cost terms: (1) cost terms defined on control points, and (2) cost terms defined via sampled states along the trajectory, and their gradients used in Section IV.

1) *Cost on Control Points*: We first consider cost terms that are expressed directly in terms of the coefficients/control points, such as integrated squared jerk. For a quintic Bézier segment  $s$  with control points  $\mathbf{c}_{s,0}, \dots, \mathbf{c}_{s,5} \in \mathbb{R}^3$ , obtained from the Hermite endpoint states via Eq. (2), the third forward differences are:  $\Delta_{s,m} = \mathbf{c}_{s,m+3} - 3\mathbf{c}_{s,m+2} + 3\mathbf{c}_{s,m+1} - \mathbf{c}_{s,m}$ ,  $m \in \{0, 1, 2\}$ . Then, the integrated squared

jerk on segment  $s$  is

$$J_{\text{smooth},s} = \int_0^{T_s} \|\mathbf{j}(t)\|^2 dt = C_s \int_0^1 \left\| \sum_{m=0}^2 \Delta_{s,m} B_m^2(\tau_s) \right\|^2 d\tau_s,$$

where  $C_s = 3600 T_s^{-5}$ . Define the (scalar) Bernstein-quadratic Gram matrix  $G \in \mathbb{R}^{3 \times 3}$  by  $G_{mn} \triangleq \int_0^1 B_m^2(\tau_s) B_n^2(\tau_s) d\tau_s$  ( $m, n = 0, 1, 2$ ), so that, with  $\Delta_s \triangleq$  then  $[\Delta_{s,0}^\top, \Delta_{s,1}^\top, \Delta_{s,2}^\top]^\top \in \mathbb{R}^9$ ,

$$J_{\text{smooth}} = \sum_{s=0}^{M-1} C_s \Delta_s^\top Q \Delta_s, \quad Q \triangleq G \otimes I_3. \quad (6)$$

(Explicitly,  $G$  is symmetric positive definite with constants  $G_{00} = G_{22} = \frac{1}{5}$ ,  $G_{11} = \frac{2}{15}$ ,  $G_{01} = G_{12} = \frac{1}{10}$ ,  $G_{02} = \frac{1}{30}$ .)

Let  $\lambda_{\min}, \lambda_{\max} > 0$  be the smallest and largest eigenvalues of  $G$ . Since  $Q = G \otimes I_3$ , the eigenvalues of  $Q$  are the eigenvalues of  $G$ , each repeated three times. Hence  $\lambda_{\min} \|\Delta_s\|^2 \leq \Delta_s^\top Q \Delta_s \leq \lambda_{\max} \|\Delta_s\|^2$ . Therefore a computationally cheap surrogate is the diagonally weighted form  $\tilde{J}_{\text{smooth}} = \sum_{s=0}^{M-1} C_s \sum_{m=0}^2 w_m \|\Delta_{s,m}\|^2$ , with fixed positive weights  $w_m$ , which is equivalent to the exact cost up to a constant factor bounded by  $\lambda_{\min}$  and  $\lambda_{\max}$ .

Now we derive  $\partial J_{\text{smooth}} / \partial \mathbf{c}$ : Each  $\Delta_{s,m}$  is an affine combination of four consecutive control points with coefficients  $\alpha_{j,m} \in \{-1, 3, -3, 1\}$  at indices  $j = m, \dots, m+3$ . Hence,  $\partial J_{\text{smooth}} / \partial \Delta_{s,m} = 2 C_s \Delta_{s,m} \partial J_{\text{smooth}} / \partial \mathbf{c}_{s,j} = 2 C_s \sum_{m=0}^2 \alpha_{j,m} \Delta_{s,m}$ . Stacking, we obtain

$$\mathbf{g}_{\mathbf{c}_s} = \frac{\partial J_{\text{smooth}}}{\partial \mathbf{c}_s} = \left[ \left( \frac{\partial J_{\text{smooth}}}{\partial \mathbf{c}_{s,0}} \right)^\top \dots \left( \frac{\partial J_{\text{smooth}}}{\partial \mathbf{c}_{s,5}} \right)^\top \right]^\top. \quad (7)$$

We can now derive  $\partial J_{\text{smooth}} / \partial T_s$ . Eq. (4) has two contributions. Since  $C_s = 3600 T_s^{-5}$ , the first contribution is

$$\frac{\partial J_s}{\partial T_s} \Big|_{\text{explicit}} = -\frac{5}{T_s} J_{\text{smooth},s}. \quad (8)$$

Using Eqs. (5) and (7), we derive the second term of Eq. (4) and obtain a closed-form expression.

2) *Cost on Sampled States*: Now we consider cost terms that are evaluated on sampled states of the trajectory. Fix a set of sample points  $\{\tau_{s,j}\}_{j=0}^{\kappa_s} \subset [0, 1]$  for segment  $s$ . Define a generic per-sample cost  $\ell: \mathbb{R}^3 \times \mathbb{R}^3 \times \mathbb{R}^3 \times \mathbb{R}^3 \times \mathbb{R}_{>0} \rightarrow \mathbb{R}$ ,  $\ell(\mathbf{x}, \mathbf{v}, \mathbf{a}, \mathbf{j}; T)$ . The sampled cost on segment  $s$  is

$$J_{\text{samp},s} = \sum_{j=0}^{\kappa_s} \ell(\mathbf{x}_s(\tau_{s,j}), \mathbf{v}_s(\tau_{s,j}), \mathbf{a}_s(\tau_{s,j}), \mathbf{j}_s(\tau_{s,j}); T_s).$$

Let the sample Jacobians at  $\tau_{s,j}$  be  $\ell_{\mathbf{x}} = \partial \ell / \partial \mathbf{x}$ ,  $\ell_{\mathbf{v}} = \partial \ell / \partial \mathbf{v}$ ,  $\ell_{\mathbf{a}} = \partial \ell / \partial \mathbf{a}$ ,  $\ell_{\mathbf{j}} = \partial \ell / \partial \mathbf{j}$ . Typically  $\ell$  has no explicit  $T_s$  (as above), so  $T_s$  appears only via time-scaling and quadrature weights.<sup>1</sup> Then, holding  $T_s$  fixed, the gradient

<sup>1</sup>If an explicit time term is desired, then  $\ell = \ell(\mathbf{x}, \mathbf{v}, \mathbf{a}, \mathbf{j}; T_s)$  and an extra  $\partial \ell / \partial T_s$  term would be added when differentiating w.r.t.  $T_s$ .

w.r.t. the  $k$ th control point is

$$\begin{aligned} \mathbf{g}_{\mathbf{c}_s, k} = & \sum_{j=0}^{\kappa_s} \left[ B_k^5 \ell_{\mathbf{x}} + \frac{5}{T_s} (B_{k-1}^4 - B_k^4) \ell_{\mathbf{v}} \right. \\ & + \frac{20}{T_s^2} (B_{k-2}^3 - 2B_{k-1}^3 + B_k^3) \ell_{\mathbf{a}} \\ & \left. + \frac{60}{T_s^3} (B_{k-3}^2 - 3B_{k-2}^2 + 3B_{k-1}^2 - B_k^2) \ell_{\mathbf{j}} \right], \end{aligned}$$

where we omit the argument of the Bernstein basis polynomials  $B(\tau_{s,j})$  for clarity. Note that  $B_r^n(\cdot) = 0$  if  $r \notin \{0, \dots, n\}$ . Stacking over  $k = 0, \dots, 5$  gives  $\mathbf{g}_{\mathbf{c}_s} = \partial J_{\text{samp},s} / \partial \mathbf{c}_s$ , which is then pulled back (chain rule) and accumulated into the Hermite variables via Eq. (3).

Changing  $T_s$  affects the sampled cost in two ways. First, (a) state-scaling: Even if we hold the Bézier control points fixed (i.e., keep the curve in normalized time  $\tau$  unchanged), rescaling  $T_s$  changes the physical derivatives via  $t = t_s + \tau_s T_s$ . Second, (b) coefficients: In Hermite parameterizations the control points themselves depend on  $T_s$  via the Hermite  $\rightarrow$  Bézier map. The two items below compute the partial derivative  $\partial J_{\text{samp},s} / \partial T_s$  for both contributions.

(a) State-scaling (fix  $\mathbf{c}_s$ ). Holding  $\mathbf{c}_s$  fixed means  $\mathbf{x}(\tau)$  is unchanged at each sample  $\tau_{s,j}$ , but  $\frac{\partial \mathbf{v}}{\partial T_s} = -\frac{1}{T_s} \mathbf{v}$ ,  $\frac{\partial \mathbf{a}}{\partial T_s} = -\frac{2}{T_s} \mathbf{a}$ ,  $\frac{\partial \mathbf{j}}{\partial T_s} = -\frac{3}{T_s} \mathbf{j}$ . Thus,

$$\frac{\partial J_{\text{samp},s}}{\partial T_s} \Big|_{\text{states}} = \sum_{j=0}^{\kappa_s} \left[ -\frac{1}{T_s} \ell_{\mathbf{v}} \mathbf{v} - \frac{2}{T_s} \ell_{\mathbf{a}} \mathbf{a} - \frac{3}{T_s} \ell_{\mathbf{j}} \mathbf{j} \right]_{\tau=\tau_{s,j}}.$$

(b) Coefficient. In Hermite parameterizations, the Bézier control points depend on  $T_s$  (e.g., tangent/curvature control points include factors of  $T_s$  and  $T_s^2$ ). Using Eq. (4) gives  $\frac{\partial J_{\text{samp},s}}{\partial T_s} \Big|_{\text{coeff}} = \mathbf{g}_{\mathbf{c}_s}^\top \frac{\partial \mathbf{c}_s}{\partial T_s}$ .

Thus, combining (a) & (b) above yields,  $\frac{\partial J_{\text{samp},s}}{\partial T_s} = \frac{\partial J_{\text{samp},s}}{\partial T_s} \Big|_{\text{states}} + \frac{\partial J_{\text{samp},s}}{\partial T_s} \Big|_{\text{coeff}}$ . Note that since generally sampling cost  $\ell$  does not depend on  $T_s$  explicitly,  $\partial J_s / \partial T_s \Big|_{\text{explicit}} = 0$ .

#### D. Reparameterizations for Derivative Variables

Each segment with duration  $T_s$  is parameterized by normalized time  $\tau_s \in [0, 1]$ ; by the chain rule,

$$\mathbf{v}(t) = \frac{\partial \mathbf{x}}{\partial t} = \frac{1}{T_s} \frac{\partial \mathbf{x}}{\partial \tau_s}, \quad \mathbf{a}(t) = \frac{\partial^2 \mathbf{x}}{\partial t^2} = \frac{1}{T_s^2} \frac{\partial^2 \mathbf{x}}{\partial \tau_s^2}.$$

Optimizing raw knot derivatives  $\{\mathbf{v}_i, \mathbf{a}_i\}$  together with  $\{T_s\}$  introduces explicit  $1/T_s$  and  $1/T_s^2$  factors in the gradients, so short segments have larger influence. We therefore optimize scaled knot derivatives. Define an averaged local time as

$$\bar{T}_i = \begin{cases} T_0, & i = 0, \\ \frac{T_{i-1} + T_i}{2}, & i = 1, \dots, M-1, \\ T_{M-1}, & i = M, \end{cases}$$

and set  $\hat{\mathbf{v}}_i = \bar{T}_i \mathbf{v}_i$ ,  $\hat{\mathbf{a}}_i = \bar{T}_i^2 \mathbf{a}_i$ . This reparameterization removes the explicit  $1/T_s$  factors from the gradients and balances sensitivity across short and long segments. Our ablation study in Section IV-C confirms the expected improvement in performance.

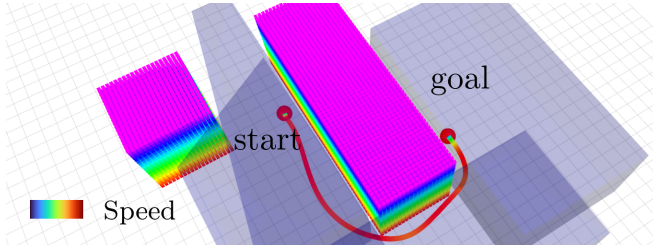


Fig. 1. Benchmarking environment for a simple corner avoidance scenario. The blue-shaded polygons show the safe flight corridor. MIGHTY’s trajectory is colored by speed (warmer colors indicate faster speeds).

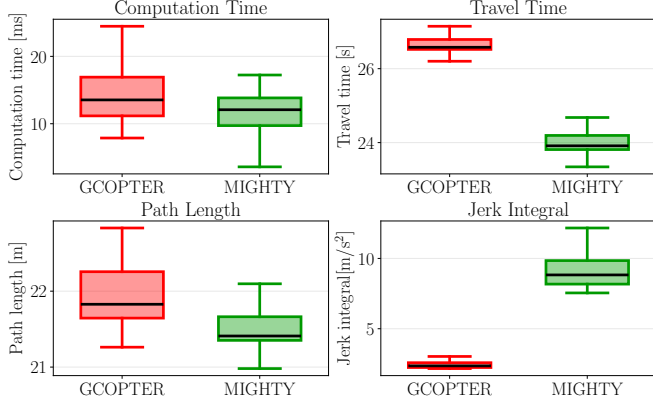


Fig. 2. Benchmarking results for MIGHTY and GCOPTER for simple corner avoidance scenario in Fig 1. MIGHTY achieves lower computation time, travel time, and path length, while GCOPTER yields lower jerk.

#### IV. SIMULATION RESULTS

All simulations were run on an AlienWare Aurora R8 with an Intel® Core™ i9-9900K CPU and 64 GB RAM, using Ubuntu 22.04 LTS and ROS 2 Humble.

##### A. Representation Benchmarking: Simple Case

We first benchmark MIGHTY against GCOPTER (which uses MINCO [19]) on a simple corner-avoidance task with fixed start and goal (Fig. 1). For a fair comparison, we implemented GCOPTER’s optimization cost in MIGHTY and use the same optimizer (L-BFGS [8]) and stopping tolerances. Both methods start from the same initial guess.

GCOPTER represents each segment as a fifth-order polynomial, so MINCO minimizes jerk (third-order effort) by construction. MIGHTY uses a fifth-order Hermite spline to match the polynomial degree. GCOPTER applies diffeomorphic parameterizations for waypoints and durations (waypoints remain inside the overlap of safe-flight corridors; durations stay positive). The only difference is that MIGHTY includes an explicit jerk smoothness term (Sec. III-C.1), while GCOPTER does not add a separate smoothness cost because MINCO already minimizes jerk.

We enforce max velocity,  $v_{\max} = 1.0 \text{ m/s}$ , max tilt angle,  $\theta_{\max} = 1.05 \text{ rad} (\approx 60^\circ)$ , max angular velocity,  $\omega_{\max} = 2.1 \text{ rad/s} (\approx 120^\circ/\text{s})$ , max  $f_{\max} = 12.0 \text{ N}$  and min  $f_{\min} = 2.0 \text{ N}$  thrust. We set  $w_T = 10^2$ ,  $w_{\text{SFC}} = 10^4$ ,  $w_v = 10^4$ ,  $w_\theta = 10^4$ ,  $w_\omega = 10^4$ , and  $w_f = 10^5$  for both MIGHTY and GCOPTER, where  $w_T$ ,  $w_{\text{SFC}}$ ,  $w_v$ ,  $w_\theta$ ,  $w_\omega$ , and  $w_f$  are weights for time, safe-flight corridor (SFC), velocity, angle, angular velocity, and thrust penalties, respectively. These match GCOPTER’s default values in their code except  $w_T$  (default 20). We use  $w_T = 10^2$  because

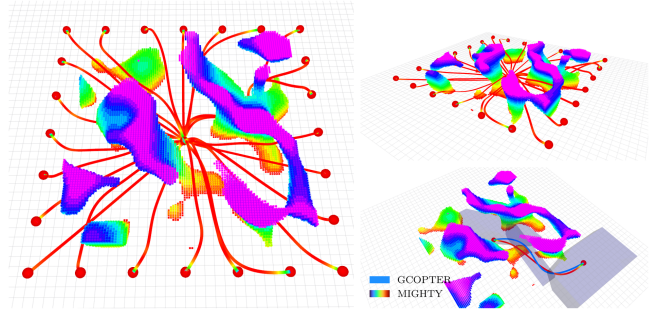


Fig. 3. Complex-scene benchmarking setup. MIGHTY’s trajectory is color-mapped by speed (warm=fast), and GCOPTER’s trajectory is blue. The start is at  $(0, 0, 0.5) \text{ m}$ , and 24 goals lie on a grid with  $x, y \in [-15, 15] \text{ m}$  and  $z = 2.5 \text{ m}$ . Blue-shaded polygons show the safe flight corridor sequence from one run.

TABLE II. Complex-scene benchmark across 24 goals and five speed limits ( $v_{\max} \in \{1, 2, 3, 4, 5\} \text{ m/s}$ ). GC = GCOPTER, MI = MIGHTY.

$v_{\max}$ [m/s]	Algo.	$T_{\text{comp}}$ [ms]	$T_{\text{trav}}$ [s]	$L_{\text{path}}$ [m]	$\int \ j(t)\  dt$ [m/s <sup>2</sup> ]	$\rho_{\text{viol}}$ [%]
1.0	GC	<b>7.7</b>	25.1	19.1	<b>2.1</b>	<b>0.0</b>
	MI	8.1 (+4.8%)	<b>21.5</b> (-14.2%)	<b>18.8</b> (-1.4%)	6.9 (+229.0%)	<b>0.0</b> (0.0%)
2.0	GC	9.8	12.6	19.0	<b>7.9</b>	<b>0.0</b>
	MI	<b>9.3</b> (-4.7%)	<b>11.0</b> (-12.8%)	<b>18.6</b> (-2.2%)	17.2 (+118.5%)	<b>0.0</b> (0.0%)
3.0	GC	11.8	8.5	19.0	<b>13.9</b>	<b>0.0</b>
	MI	<b>7.8</b> (-33.6%)	<b>7.7</b> (-9.8%)	<b>18.7</b> (-1.4%)	27.2 (+95.9%)	<b>0.0</b> (0.0%)
4.0	GC	7.7	6.9	18.8	<b>17.6</b>	<b>0.0</b>
	MI	<b>7.2</b> (-5.5%)	<b>6.0</b> (-13.0%)	<b>18.6</b> (-1.2%)	35.6 (+102.6%)	<b>0.0</b> (0.0%)
5.0	GC	<b>6.8</b>	6.1	18.8	<b>19.8</b>	<b>0.0</b>
	MI	7.2 (+5.7%)	<b>5.3</b> (-14.1%)	<b>18.7</b> (-0.7%)	43.7 (+120.5%)	<b>0.0</b> (0.0%)
<b>Overall</b>		<b>-9.3%</b>	<b>-13.1%</b>	<b>-1.4%</b>	+113.3%	0.0%

$w_T = 10^3$  caused occasional constraint violations ( $> 1\%$ ) in GCOPTER. For MIGHTY, we set the jerk smoothness weight to  $w_{\text{smooth}} = 10^{-5}$ . GCOPTER sets yaw to the direction of motion, so yaw and yaw rate are determined by  $\mathbf{p}$ . Accordingly, although neither GCOPTER nor MIGHTY optimizes yaw directly, both penalize tilt angle and angular velocity. We configure MIGHTY this way solely for fair comparison with GCOPTER. Outside this benchmark (see Sec. IV-D), MIGHTY can use a different cost design.

The result summary in Fig. 2 shows that MIGHTY achieves a shorter travel time, with slightly faster computation and shorter path than GCOPTER. While GCOPTER produces smoother trajectories with lower jerk due to its constraint within the MINCO manifold, MIGHTY explores a larger search space to identify faster and more effective trajectories. This flexibility enables MIGHTY to achieve superior overall performance.

##### B. Representation Benchmarking: Complex Case

We further evaluate MIGHTY in a complex environment (Fig. 3). The start is fixed at  $(0, 0, 0.5) \text{ m}$ . For each  $v_{\max} \in \{1, 2, 3, 4, 5\} \text{ m/s}$ , we plan to 24 goal locations with  $x, y \in [-15, 15] \text{ m}$  and  $z = 2.5 \text{ m}$ . Optimization settings are identical to the simple case for both methods. We report the following metrics:  $v_{\max}$  [m/s]: Speed limit,  $T_{\text{comp}}$  [ms]: Computation time,  $T_{\text{trav}}$  [s]: Travel time,  $L_{\text{path}}$  [m]: Path

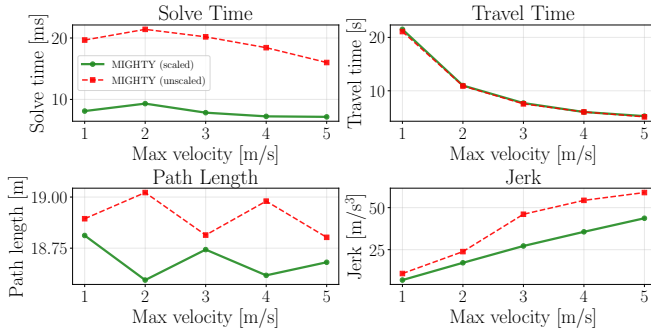


Fig. 4. Ablation study comparing MIGHTY with scaled and unscaled variables in the complex benchmarking scenario. The scaled version shows  $\approx 2\times$  faster computation time, with lower jerk and slightly shorter path length, while travel time is nearly identical.

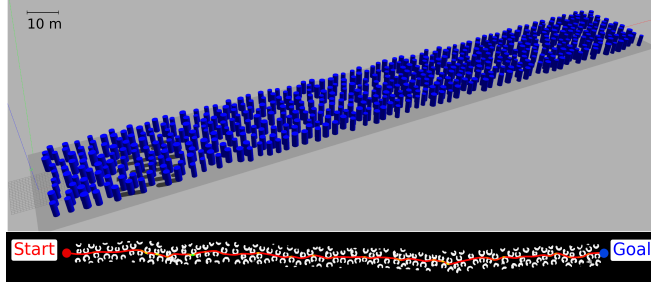


Fig. 5. (Top) Static obstacle environment used for benchmarking. (Bottom) Top view of the point cloud and path generated by MIGHTY in the static environment. The warmer colors indicate faster speeds.

length,  $\int \|\mathbf{j}(t)\| dt$  [m/s<sup>2</sup>]: Jerk smoothness integral, and  $\rho_{\text{viol}}$  [%]: Fraction of time violating dynamic bounds.

Overall, Table II shows that MIGHTY reduces computation time by **9.3%**, travel time by **13.1%**, and path length by **1.4%** relative to GCOPTER. Consistent with the simple case, GCOPTER yields a lower jerk integral, while MIGHTY's higher jerk reflects more aggressive, time-efficient maneuvers. Both planners keep  $\rho_{\text{viol}} \leq 1.0\%$ .

### C. Ablation Study on Scaled and Unscaled Variables

As discussed in Section III-D, we optimize over scaled variables to improve numerical stability. We evaluate this with an ablation between MIGHTY (scaled) and an unscaled variant. As in the complex benchmarking, both run in the same environment with 24 goals for  $v_{\text{max}} \in \{1, \dots, 5\}$  m/s, using identical objectives, constraints, initial guess, and solver settings. Fig. 4 shows that the scaled variant is about  $2\times$  faster in computation time, with lower jerk, while path length and travel time are nearly identical. These results confirm that scaling improves numerical stability and optimization efficiency without degrading trajectory quality.

### D. Benchmarking in Static Environments

To thoroughly evaluate MIGHTY, we benchmark it in an obstacle-rich environment (Fig. 5) against EGO-Swarm [24], EGO-Swarm2 [23], and SUPER [14]. Static cylindrical obstacles are placed randomly with radii sampled in [1.0 m, 1.5 m] and height 6.0 m, occupying a 300 m  $\times$  40 m area. The agent starts at (0, 0, 3) m and the goal is (305, 0, 3) m. We constrain velocity, acceleration, and jerk to  $v_{\text{max}} = 4.0$  m/s,  $a_{\text{max}} = 10.0$  m/s<sup>2</sup>, and  $j_{\text{max}} = 30.0$  m/s<sup>3</sup>. For global guidance we run JPS [5], then build a safe-flight corridor (SFC) [9] for local optimization.

For soft constraints we use a smooth hinge  $\phi_{\mu}(\cdot)$ . Time integrals are evaluated by trapezoidal quadrature with  $\kappa$  samples per segment unless a closed form is available. Safe-flight corridors (SFCs) are modeled per segment  $s$  as the intersection of halfspaces

$\text{SFC}_s \triangleq \{\mathbf{x} \in \mathbb{R}^3 \mid \mathbf{a}_{s,h}^{\top} \mathbf{x} \leq b_{s,h} - C_{\text{SFC}}, h = 1, \dots, H_s\}$ , where  $H_s$  is the number of halfspaces on segment  $s$ , and  $C_{\text{SFC}} = 0.2$  is a safety margin. The total objective is

$$J = w_T \sum_s T_s + w_{\text{smooth}} \tilde{J}_{\text{smooth}} + w_{\text{SFC}} J_{\text{SFC}} \\ + w_v J_v + w_a J_a + w_j J_j,$$

where  $J_{\text{SFC}} = \sum_s \int_0^{T_s} \sum_{h=1}^{H_s} \phi_{\mu}(\mathbf{a}_{s,h}^{\top} \mathbf{x}(t) - b_{s,h} + C_{\text{SFC}}) dt$ , penalizes leaving the SFC,  $J_v = \sum_s \int_0^{T_s} \phi_{\mu}(\|\mathbf{v}(t)\|^2 - v_{\text{max}}^2) dt$ ,  $J_a = \sum_s \int_0^{T_s} \phi_{\mu}(\|\mathbf{a}(t)\|^2 - a_{\text{max}}^2) dt$ , and  $J_j = \sum_s \int_0^{T_s} \phi_{\mu}(\|\mathbf{j}(t)\|^2 - j_{\text{max}}^2) dt$ . Note that the jerk smoothness cost  $\tilde{J}_{\text{smooth}}$  uses the closed form given in Eq. 6, which avoids per-sample recomputation. MIGHTY's weights are  $w_T = 5 \times 10^2$ ,  $w_{\text{smooth}} = 10^{-1}$ ,  $w_{\text{SFC}} = 10^3$ ,  $w_v = 10^3$ ,  $w_a = 10^3$ ,  $w_j = 10^3$ . We run 10 trials per method. **Metrics:**  $R_{\text{succ}}$  [%] (success rate; collision-free, reaches goal);  $T_{\text{opt}}$  [ms] (local optimization time);  $T_{\text{total}}$  [ms] (total planning time);  $T_{\text{trav}}$  [s] (travel time);  $L_{\text{path}}$  [m] (path length);  $S_{\text{jerk}} = \int \|\mathbf{j}(t)\| dt$  [m/s<sup>3</sup>] (smoothness);  $\bar{S}_{\text{jerk}} = \sqrt{\frac{1}{T} \int \|\mathbf{j}(t)\|^2 dt}$  [m/s<sup>3</sup>] (RMS jerk; time-normalized);  $\rho_{\text{vel}}$ ,  $\rho_{\text{acc}}$ ,  $\rho_{\text{jerk}}$  [%] (velocity/acceleration/jerk violations). We report  $\bar{S}_{\text{jerk}}$  to account for differing travel times across methods.

Fig. 5 illustrates the environment and one MIGHTY trajectory (in red in the bottom plot), and Table III gives the full results. We evaluate each method with its default sensor; for methods whose default is not LiDAR (EGO-Swarm, EGO-Swarm2), we also run a LiDAR variant to align with SUPER and MIGHTY (both LiDAR-based). Note that EGO-Swarm with LiDAR performed substantially worse, so Table III omits those data for clarity. For EGO-Swarm,  $v_{\text{max}} = 4.0$  m/s yielded a 40% success rate; reducing  $v_{\text{max}}$  to 3.0 m/s to 1.0 m/s improved safety, reaching up to 90% at 1.0 m/s. For EGO-Swarm2, with depth-camera input, it achieves 100% success and low compute time at both obstacle weights  $w_{\text{obst}} \in \{1 \times 10^4, 5 \times 10^4\}$ . With LiDAR input, the success rates are 20% and 70% at the same weights. For SUPER,  $w_t = 10^4$  gave 20% success, and reducing  $w_t$  to  $10^1$  achieved 100%. Note that SUPER applies a soft penalty on the distance between the trajectory and points in the overlap of successive SFC segments, with weight  $5 \times 10^6$ , which is the largest among all cost terms. Summarizing the results, we see that EGO-Swarm2 is the fastest in local optimization and total replanning time (**0.7 ms** and **1.0 ms**), whereas MIGHTY achieves the shortest travel time (**79.0 s**) and path length (**310.9 m**). The jerk of MIGHTY is higher ( $S_{\text{jerk}} = 522.2$  m/s<sup>3</sup>,  $\bar{S}_{\text{jerk}} = 9.4$  m/s<sup>3</sup>); however, this is consistent with prior observations of the trade-off between performance and smoothness.

### E. Dynamic Environments

TABLE III. Benchmarking results (safety, computation time, performance, and constraint violation). We mark in **green** the best value in each column *considering only configurations with  $R_{\text{succ}} = 100\%$* ; configurations with  $R_{\text{succ}} < 100\%$  are excluded from best highlighting. For EGO-Swarm2, we evaluated both its default sensor, depth camera, and a LiDAR (as used by SUPER and MIGHTY) and report results as “camera” | “LiDAR”. We also tested EGO-Swarm with LiDAR, but its performance was substantially worse, so we omit it from the table for clarity. For SUPER, computation time is reported as “exploratory” & “safe”. The data are shaded red if they have unsuccessful rates  $R_{\text{succ}} < 100\%$ .

Algorithm	Params	Traj.	Success	Computation Time			Performance				Constraint Violation		
			$R_{\text{succ}} [\%]$	$T_{\text{opt}} [\text{ms}]$	$T_{\text{total}} [\text{s}]$	$T_{\text{trav}} [\text{s}]$	$L_{\text{path}} [\text{m}]$	$S_{\text{jerk}} [\text{m/s}^2]$	$\bar{S}_{\text{jerk}} [\text{m/s}^3]$	$\rho_{\text{vel}} [\%]$	$\rho_{\text{acc}} [\%]$	$\rho_{\text{jerk}} [\%]$	
EGO-Swarm	$v_{\text{max}} = 4.0 \text{ m/s}$	B-spline	<b>40.0</b>	1.8	2.3	135.9	379.7	4233.1	43.6	3.5	6.5	38.0	
	$v_{\text{max}} = 3.0 \text{ m/s}$		<b>70.0</b>	1.8	2.4	178.2	380.2	3024.5	26.7	5.7	1.2	16.5	
	$v_{\text{max}} = 2.0 \text{ m/s}$		<b>80.0</b>	0.9	1.3	262.7	364.8	1074.9	7.3	3.8	0.01	0.4	
	$v_{\text{max}} = 1.0 \text{ m/s}$		<b>90.0</b>	0.6	0.9	559.8	370.0	204.4	0.6	0.1	0.0	0.0	
EGO-Swarm2	$w_{\text{obst}} = 1 \times 10^4$	MINCO	<b>100.0</b>   <b>20.0</b>	1.3   5.9	1.8   7.6	144.7   144.6	329.8   331.7	263.3   336.8	2.5   3.5	<b>0.0</b>   <b>0.6</b>	<b>0.0</b>   <b>0.0</b>	<b>0.0</b>   <b>0.01</b>	
	$w_{\text{obst}} = 1 \times 10^5$		<b>100.0</b>   <b>70.0</b>	<b>1.2</b>   4.6	<b>1.7</b>   5.9	140.2   150.1	326.9   333.5	243.2   247.7	2.2   3.5	0.05   0.02	<b>0.0</b>   <b>0.0</b>	<b>0.0</b>   <b>0.0</b>	
SUPER	$w_t = 1 \times 10^4$	MINCO	<b>20.0</b>	5.9 & 18.0	46.4	87.5	323.5	627.4	10.9	0.0	0.02	1.0	
	$w_t = 1 \times 10^3$		<b>60.0</b>	5.6 & 18.0	57.5	99.6	323.4	431.9	6.7	0.0	0.02	0.2	
	$w_t = 1 \times 10^2$		<b>60.0</b>	6.8 & 18.2	47.6	124.7	326.9	399.5	4.2	0.0	0.01	0.06	
	$w_t = 1 \times 10^1$		<b>100.0</b>	7.8 & 18.9	50.6	264.7	342.0	<b>200.0</b>	<b>0.9</b>	<b>0.0</b>	<b>0.0</b>	<b>0.0</b>	
MIGHTY		Hermite	<b>100.0</b>	10.5	19.7	<b>79.0</b>	<b>310.9</b>	522.2	9.4	<b>0.0</b>	<b>0.0</b>	<b>0.0</b>	

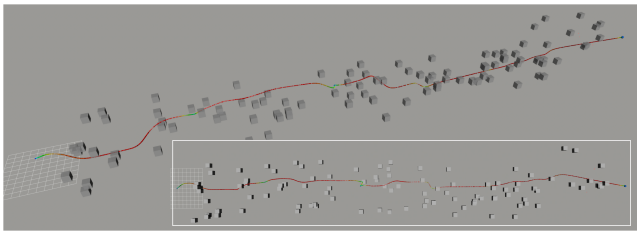


Fig. 6. Benchmarking scenario with 100 dynamic obstacles following smooth trefoil-knot trajectories. The image shows the agent’s trajectory

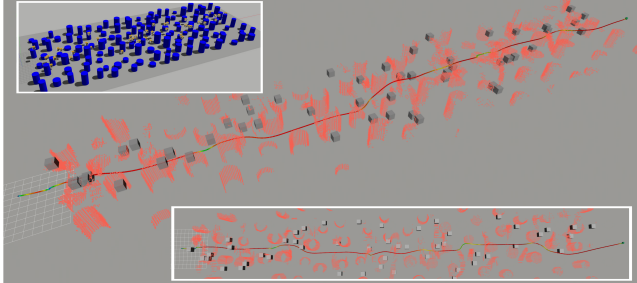


Fig. 7. Benchmarking scenario with 50 dynamic obstacles and static obstacles. The top left image illustrates the Gazebo simulation environment. The main image and bottom right image show the point cloud (pink-orange) and agent’s trajectory (color-mapped by speed) navigating through both static and dynamic obstacles.

We further evaluate MIGHTY in two dynamic scenarios: (1) only dynamic obstacles, and (2) dynamic & static obstacles. For both, in addition to the cost terms described in Section IV-D, we add a dynamic-obstacle avoidance cost  $J_{\text{dyn}} = \int_0^{\sum_s T_s} (C_{\text{dyn}}^2 - \|\mathbf{x}(t) - \mathbf{k}(t)\|^2)_+^3 dt$ , where  $\mathbf{k}(t)$  is the position of a dynamic obstacle at time  $t$ , and  $(\cdot)_+ = \max(0, \cdot)$ . We set the weight  $w_{\text{dyn}} = 10^1$  and use a soft barrier radius  $C_{\text{dyn}} = 3.0 \text{ m}$ . Note that  $C_{\text{dyn}}$  is where the penalty activates, not a hard safety distance. The robot collision radius is 0.1 m. The start and goal are  $(0, 0, 3) \text{ m}$  and  $(100, 0, 3) \text{ m}$ , and, in this more complex environment, the dynamic constraints are set to  $v_{\text{max}} = 2.0 \text{ m/s}$ ,  $a_{\text{max}} = 5.0 \text{ m/s}^2$ , and  $j_{\text{max}} = 30.0 \text{ m/s}^3$ .

**Dynamic-only environment:** We generate 100 dynamic obstacles following smooth trefoil-knot trajectories, with initial positions  $x \in [0, 100] \text{ m}$ ,  $y \in [-10, 10] \text{ m}$ ,  $z \in [1, 6] \text{ m}$ . Fig. 6 shows an example of the environment and the

TABLE IV. Nearest dynamic-obstacle distances by environment for 10 runs each. Columns show 0th (min), 5th, 50th (median), and 95th percentiles. The robot collision radius is set to 0.1 m.

Environment	Distance [m]			
	0th (min)	5th	50th (median)	95th
Only Dynamic	0.8	2.1	3.2	5.2
Dynamic + Static	1.0	2.5	3.8	6.8

trajectory. MIGHTY avoids all obstacles in **10/10** trials. As shown in Table IV, the minimum nearest-obstacle distance is 0.8 m, above the 0.1 m safety threshold.

**Dynamic & static environment:** We add 50 dynamic obstacles (same motion model) to the static forest as shown in Fig. 7 and run 10 trials. MIGHTY avoids all obstacles in **all trials**. Table IV summarizes nearest-obstacle distances, where the minimum is 1.0 m, above the 0.1 m.

## V. HARDWARE EXPERIMENTS

We also evaluated MIGHTY in three hardware experiment: (1) long-duration flights at  $v_{\text{max}} \in \{1, 2, 3, 4\} \text{ m/s}$ , (2) high-speed flights up to  $v_{\text{max}} = 7 \text{ m/s}$ , and (3) flights with obstacles introduced during the mission. The perception uses a Livox Mid-360 LiDAR, and localization is provided by DLIO [2]. Planning runs onboard on an Intel<sup>TM</sup> NUC 13, and low-level control uses PX4 [10] on a Pixhawk flight controller [11]. All perception, planning, and control run in real time onboard.

**Long-Duration Flight Experiment:** To assess reliability over extended operations, the vehicle repeatedly traverses a space with multiple obstacles (Fig. 8). Six goal positions are placed opposite the start, inducing repeated out-and-back motions through the environment. For  $v_{\text{max}} \in \{1, 2, 3, 4\} \text{ m/s}$ , all flights completed without collision.

**High-Speed Flight Experiment:** We further evaluate performance at higher speeds. As shown in Section IV, MIGHTY tends to produce higher-jerk trajectories; when constraints are satisfied, these trajectories remain safe while enabling faster motion. We test  $v_{\text{max}} = 5.0 \text{ m/s}, 6.0 \text{ m/s}, 7.0 \text{ m/s}$ . Figure 9 shows the resulting histories. All flights completed without collision, demonstrating that the MIGHTY planner and DLIO state estimation operate effectively at high speed. At  $v_{\text{max}} = 7.0 \text{ m/s}$ , the vehicle reached **6.7 m/s** peak speed.

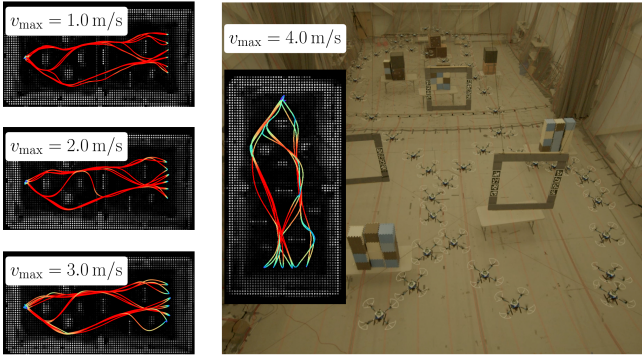


Fig. 8. Long-duration experiment with  $v_{\max} \in \{1, 2, 3, 4\} \text{ m/s}$ . Top: partial action sequence at  $v_{\max} = 4.0 \text{ m/s}$  (cropped for clarity). Bottom: full trajectory histories overlaid on the recorded LiDAR point cloud. Warmer colors indicate higher speed (red:  $v_{\max}$ , blue: 0.0 m/s); white points are the onboard point cloud.

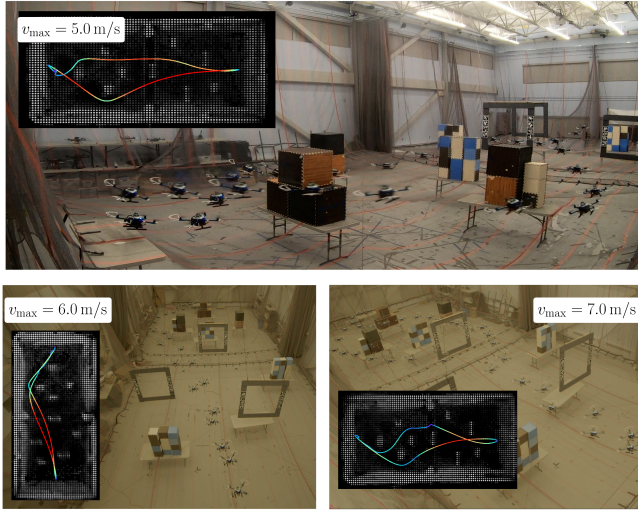


Fig. 9. High-speed experiments at  $v_{\max} = 5.0 \text{ m/s}, 6.0 \text{ m/s}, 7.0 \text{ m/s}$ . Each panel shows the action sequence with trajectory history over the recorded point cloud. Warmer colors indicate higher speed (red:  $v_{\max}$ , blue: 0.0 m/s); white points are the onboard point cloud.

**Dynamic Obstacle Flight Experiment:** To assess robustness to changes in the environment, we introduce and move obstacles during the mission (Fig. 10). We track a person carrying obstacles and incorporate the estimates into the trajectory optimization; see Section IV-E for details. The agent successfully avoids all obstacles and reaches the goal without collision over 490 s of flight time.

## VI. CONCLUSIONS

We presented MIGHTY, a Hermite-spline trajectory planner for joint spatiotemporal optimization. By optimizing path geometry and time together with local derivative control, MIGHTY generates smooth, collision-free, and dynamically feasible trajectories for high-performance maneuvers. Benchmarks and hardware tests show MIGHTY outperforms baselines in travel time while satisfying constraints.

## VII. ACKNOWLEDGEMENTS

The authors would like to thank Lili Sun for her help with the hardware experiments and Mason B. Peterson for his support with *robotdata.py* library. The authors also thank Juan Rached for his help with hardware setup. This work

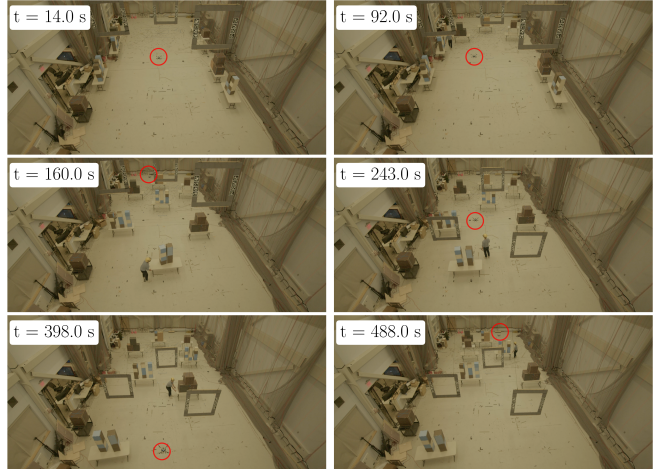


Fig. 10. Dynamic-environment experiment at  $v_{\max} = 1.0 \text{ m/s}$ . The red circle shows the UAV; obstacles are introduced and moved during flight.

was supported in part by DSTA and ARL grant W911NF-21-2-0150.

## REFERENCES

- [1] Michael Burri, Helen Oleynikova, Markus W. Achtelik, and Roland Siegwart. Real-time visual-inertial mapping, re-localization and planning onboard mavs in unknown environments. In *2015 IEEE/RSJ International Conference on Intelligent Robots and Systems (IROS)*, pages 1872–1878, 2015.
- [2] Kenny Chen, Ryan Nemiroff, and Brett T Lopez. Direct lidar-inertial odometry: Lightweight lio with continuous-time motion correction. In *2023 IEEE international conference on robotics and automation (ICRA)*, pages 3983–3989. IEEE, 2023.
- [3] Robin Deits and Russ Tedrake. Efficient mixed-integer planning for uavs in cluttered environments. In *2015 IEEE International Conference on Robotics and Automation (ICRA)*, pages 42–49, 2015.
- [4] Michel Fliess, Jean Lévine, Philippe Martin, and Pierre Rouchon. Flatness and defect of non-linear systems: introductory theory and examples. *International Journal of Control*, 61(6):1327–1361, 1995.
- [5] Daniel Harabor and Alban Grastien. Online graph pruning for pathfinding on grid maps. In *Proceedings of the AAAI conference on artificial intelligence*, 2011.
- [6] Kota Kondo, Mason Peterson, Nicholas Rober, Juan Rached Viso, Lucas Jia, Jialin Chen, Harvey Merton, and Jonathan P How. Dynus: Uncertainty-aware trajectory planner in dynamic unknown environments. *arXiv preprint arXiv:2504.16734*, 2025.
- [7] Helene J Levy and Brett T Lopez. Stitcher: Real-time trajectory planning with motion primitive search. *arXiv preprint arXiv:2412.21180*, 2024.
- [8] Dong C Liu and Jorge Nocedal. On the limited memory bfgs method for large scale optimization. *Mathematical programming*, 45(1):503–528, 1989.
- [9] Sikang Liu, Michael Watterson, Kartik Mohta, Ke Sun, Subhrajit Bhattacharya, Camillo J Taylor, and Vijay Kumar. Planning dynamically feasible trajectories for quadrotors using safe flight corridors in 3-d complex environments. *RA-L*, 2(3):1688–1695, 2017.
- [10] Lorenz Meier, Dominik Honegger, and Marc Pollefeys. Px4: A node-based multithreaded open source robotics framework for deeply embedded platforms. In *2015 IEEE International Conference on Robotics and Automation (ICRA)*, pages 6235–6240, 2015.
- [11] Lorenz Meier, Petri Tanskanen, Friedrich Fraundorfer, and Marc Pollefeys. Pixhawk: A system for autonomous flight using onboard computer vision. In *2011 IEEE International Conference on Robotics and Automation*, pages 2992–2997, 2011.
- [12] Daniel Mellinger and Vijay Kumar. Minimum snap trajectory generation and control for quadrotors. In *2011*, pages 2520–2525, 2011.
- [13] Helen Oleynikova, Michael Burri, Zachary Taylor, Juan Nieto, Roland Siegwart, and Enric Galceran. Continuous-time trajectory optimization for online uav replanning. In *2016 IEEE/RSJ International Conference on Intelligent Robots and Systems (IROS)*, pages 5332–5339, 2016.

- [14] Yunfan Ren, Fangcheng Zhu, Guozheng Lu, Yixi Cai, Longji Yin, Fanze Kong, Jiarong Lin, Nan Chen, and Fu Zhang. Safety-assured high-speed navigation for mavs. *Science Robotics*, 10(98):eado6187, 2025.
- [15] Charles Richter, Adam Bry, and Nicholas Roy. Polynomial trajectory planning for aggressive quadrotor flight in dense indoor environments. In *Robotics Research: The 16th International Symposium ISRR*, pages 649–666. Springer, 2016.
- [16] Weidong Sun, Gao Tang, and Kris Hauser. Fast uav trajectory optimization using bilevel optimization with analytical gradients. In *2020 American Control Conference (ACC)*, pages 82–87, 2020.
- [17] Jesus Tordesillas, Brett T. Lopez, Michael Everett, and Jonathan P. How. Faster: Fast and safe trajectory planner for navigation in unknown environments. *IEEE Transactions on Robotics*, 38(2):922–938, 2022.
- [18] Zhepei Wang, Hongkai Ye, Chao Xu, and Fei Gao. Generating large-scale trajectories efficiently using double descriptions of polynomials. In *IEEE International Conference on Robotics and Automation*, pages 7436–7442, Xi'an, China, 2021. IEEE.
- [19] Zhepei Wang, Xin Zhou, Chao Xu, and Fei Gao. Geometrically constrained trajectory optimization for multicopters. *IEEE Transactions on Robotics*, 38(5):3259–3278, 2022.
- [20] Boyu Zhou, Fei Gao, Luqi Wang, Chuhao Liu, and Shaojie Shen. Robust and efficient quadrotor trajectory generation for fast autonomous flight. *RA-L*, 4(4):3529–3536, 2019.
- [21] Boyu Zhou, Jie Pan, Fei Gao, and Shaojie Shen. Raptor: Robust and perception-aware trajectory replanning for quadrotor fast flight. *T-RO*, 37(6):1992–2009, 2021.
- [22] Xin Zhou, Zhepei Wang, Hongkai Ye, Chao Xu, and Fei Gao. EGO-Planner: An ESDF-Free Gradient-Based Local Planner for Quadrotors. *IEEE Robotics and Automation Letters*, 6(2):478–485, 2021.
- [23] Xin Zhou, Xiangyong Wen, Zhepei Wang, Yuman Gao, Haojia Li, Qianhao Wang, Tiankai Yang, Haojian Lu, Yanjun Cao, Chao Xu, et al. Swarm of micro flying robots in the wild. *Science Robotics*, 7(66):eabm5954, 2022.
- [24] Xin Zhou, Jiangchao Zhu, Hongyu Zhou, Chao Xu, and Fei Gao. Ego-swarm: A fully autonomous and decentralized quadrotor swarm system in cluttered environments. In *2021 IEEE ICRA*, pages 4101–4107. IEEE, 2021.